



Gas sensing performance of Ni-doped CuO/ZnO p–n heterostructures for ethanol detection: high sensitivity, selectivity and stability

Fatma Janene^{1,*} , Ali Moulahi^{2,3}, Fathi Touati¹, and Hassouna Dhaouadi¹

¹ Laboratoire Matériaux Traitement et Analyse, National Research Institute of Physical and Chemical Analysis, Technological Pole Sidi Thabet, 2020 Sidi Thabet, Tunisia

² Department of Chemistry, Alwajh College, University of Tabuk, Tabuk 71421, Saudi Arabia

³ Unit of Materials and Environment (UR15ES01), IPEIT, University of Tunis, Tunis, Tunisia

Received: 5 July 2023

Accepted: 26 August 2023

Published online:

11 September 2023

© The Author(s), under exclusive licence to Springer Science+Business Media, LLC, part of Springer Nature, 2023

ABSTRACT

The gas sensitive characteristics of pure, 4 and 6 wt% Ni-doped CuO/ZnO nanocomposites toward ethanol gas were studied for industrial and safety applications. The X-ray diffraction analysis verified that the pure, 4 and 6 wt% Ni-doped CuO/ZnO nanocomposites were composed of monoclinic CuO and hexagonal ZnO phases without existence of any impurities. The scanning electron microscope image of pure CuO/ZnO powder shows the formation of uniform and well distribution spherical particles. Owing to incorporation of Ni ions, some rods particles were formed besides major fine semi-spherical grains. Pure CuO/ZnO exhibits two band gap energies with value of 1.4 and 3.2 eV which can be exactly indexed to CuO and ZnO components, respectively. Upon doping by Ni ions, the band gap of p-type CuO was blue shifted, while the band gap of the n-type ZnO was red shifted. The gas sensing performance of CuO/ZnO heterostructure shows a maximum sensitivity at 250 °C towards 100 ppm ethanol gas while Ni-doped CuO/ZnO nanocomposites attain a maximum sensitivity at 225 °C. The measurements revealed that the 4 wt% Ni-doped CuO/ZnO possesses superior gas sensing characteristics including high response, fast response and recovery times as well as good stability towards 100 ppm ethanol gas. Besides, this sensor exhibits high selectivity for ethanol gas in presence of many volatile organic compounds such as acetone, formaldehyde, methanol and propanol as well as carbon dioxide. This work indicates that Ni-doped CuO/ZnO heterojunction is a highly promising sensitive structure for ethanol gas detection.

Address correspondence to E-mail: janene.fatma@yahoo.fr

1 Introduction

Design and synthesis of highly sensitive gas sensing compositions are interesting research topic for different fields such as environmental monitoring [1], food industry production [2], toxic, flammable and explosive safety [3–5] and medical diagnosis applications [6]. Innovative scientific efforts to achieve high response, remarkable stability, high selectivity and fast response/recovery time for superior performance gas sensing devices [7, 8]. Numerous volatile organic compounds (VOCs) such as methanol, ethanol, formaldehyde, acetone, benzene, toluene and xylene are released from industries and laboratories activities; these compounds possess strong toxicity to human health and can even lead to death [9–11]. Ethanol ($\text{CH}_3\text{CH}_2\text{OH}$) is an important industrial chemical volatile organic compound due to its daily usage in many fields such as food, paints, cosmetics, alcoholic beverages, pharmaceutical and chemical products industries [12–14]. Continued exposure to high concentration of ethanol compound can induce irritation of eyes, nose and mucous membranes in addition to nausea, vertigo and headaches [14, 15]. Furthermore, the consumption of ethanol is a main reason of frequent traffic accidents due to drunk driving [16]. For car drivers, the allowable concentrations of ethanol are 208 ppm in the exhaled air and 130 ppm (parts per million) in the blood (0.05%) [17]. Due to these reasons, the fabrication of high performance and low cost ethanol gas sensors is an important subject.

In last years, many types of gas sensors for ethanol gas detection have been developed such as surface acoustic wave sensor [18], electrochemical sensor [19] and resistive sensor [20]. Among these types of sensors, the semiconducting metal oxides (MOs) resistive gas sensors have gained the great interest owing to easy fabrication, low cost, simplicity of use, ability to detect different types of gases including toxic and flammable gases as well as volatile organic compounds [2, 21, 22]. The metal oxide materials are typically classified into p-type and n-type semiconductors with majority of charge carriers including holes and electrons, respectively [21]. The sensing performances of the p-type and n-type metal oxide semiconductors are opposite due to the difference of the conducting mechanism [21]. Many strategies were employed to improve the gas sensing characteristics of the pure metal oxides including doping [23], codoping [24, 25], micro/nanostructured design [26], altering

morphology [27] and p–n heterojunction formation [28, 29]. The heterostructures made between p and n-types metal oxide semiconductors as well as doping technique are more effective owing to the opportunity of integration between physical and chemical characteristics [30–32].

Numerous metal oxide semiconductors heterostructures have been studied including ZnO/CuO heterojunction for ammonia gas detection [33]. ZnO/CuO and $\text{Co}_3\text{O}_4/\text{AlOOH}$ composites for detection of H_2S and NO_x [34, 35]. Gao et al. [36] and Ji et al. [37] have been investigated the gas sensing characteristics of Au/CuO/ Cu_2O and $\text{Co}_3\text{O}_4/\text{In}_2\text{O}_3$ heterostructures for triethylamine gas detection. For ethanol detection, the gas sensing properties of heteroassembly of n-type $\alpha\text{-Fe}_2\text{O}_3$ nanoparticles on a p-type LaFeO_3 matrix into a pore-rich hollow nanostructure have been investigated by Zhou et al. [38]. Also, the gas sensing properties of CuO–ZnO composite have been studied for detection of CO_2 [39], humidity [40], formaldehyde [41], CO [42], N-butanol [43] and hydrogen sulfide [44]. Ren et al. studied the gas sensitivity of porous sea-urchin-like CuO/ZnO composite nanostructure towards acetone, ethanol and formaldehyde [45]. They found that the sea-urchin-like CuO/ZnO composite has a sensitivity value of 52.6 and 48 at working temperature of 220 °C for acetone and ethanol, respectively. Liu et al. [46] reported enhanced ethanol gas sensing properties of ultrathin ZnO nanosheets decorated with CuO nanoparticles with measured sensitivity value of 130 (concentration 200 ppm) at operating temperature of 320 °C. The gas sensing characteristics of flower-like p-CuO/n-ZnO heterojunction nanorods were measured for ethanol gas detection [47]. The measurements reveal that the p-CuO/n-ZnO heterojunction sensor has response value of 98.8 for 100 ppm ethanol at temperature of 300 °C. The room temperature gas sensing properties of ZnO–CuO heterojunction prepared by hydrothermal method show a response value of 3.3 to 200 ppm ethanol vapor [48]. Qin et al. investigated the gas sensitive features of CuO–ZnO/g- C_3N_4 ternary composite for ethanol gas at different temperatures [49]. Their results indicate that CuO–ZnO/g- C_3N_4 sensor has a sensitivity of 15.6 at 260 °C for concentration of 500 ppm ethanol. Akbari-Saatlu et al. [50] showed that the ZnO/ SnO_2 heterostructures grown on alumina has a high sensitivity of 172 to 5 ppm H_2S gas at 450 °C. On the other hand, the p–n junctions composed of CuO-decorated ZnO nanowires for ethanol gas sensing applications were

synthesized by Zhao et al. [51]. They found that the maximum response was realized at 300 °C with sensitivity value of nearly 28 for 100 ppm ethanol vapor.

According to our knowledge, no available study on the influence of Ni doping on the gas sensing properties of CuO–ZnO p–n heterojunction for ethanol gas detection. Ni as a transition metal dopant can promote the active sites formation and favoring the adsorption of oxygen species which can enhance the gas sensitive properties of CuO–ZnO p–n heterojunction. Besides that, the Ni as a transition metal dopant can activate the sensing reaction at low operating temperature. The integration between the strategy of p–n heterojunction formation and doping technique can lead to advanced sensing properties. In this study, new gas sensor compositions composed of 4 and 6 wt% Ni-doped CuO–ZnO p–n heterojunction were prepared using the sol–gel technique. The crystal structure, morphological and optical properties of the synthesized samples have been characterized by X-ray diffraction (XRD), scanning electron microscope (SEM), energy dispersive spectroscopy (EDS), Fourier-transform infrared (FTIR) and diffuse reflectance spectroscopy. The gas sensing performance of pure, 4 and 6 wt% Ni-doped CuO–ZnO p–n heterojunction has been investigated on pellet form with contact by silver electrodes for ethanol gas detection. The gas sensing characteristics like sensitivity, selectivity, response time and recovery time have been estimated as well as the possible mechanism for detection has been discussed. The obtained results illustrate that 4 wt% Ni-doped CuO/ZnO sensor has a high sensitivity of 97 towards 100 ppm ethanol gas with high selectivity at operating temperature 225 °C. This sensor exhibits good linear relation between sensitivity and ethanol gas concentration within 50–250 ppm with a fast response time of 20 s and small recovery time of 15 s with excellent stability for 28 days. At room temperature, 4 wt% Ni-doped CuO/ZnO sensor exhibits a good response value of 6.1 to 100 ppm ethanol gas.

2 Experimental

2.1 Preparation of pure and Ni-doped CuO/ZnO nanocomposites

Copper nitrate trihydrate ($\text{Cu}(\text{NO}_3)_2 \cdot 3\text{H}_2\text{O}$, 99%), zinc nitrate hexahydrate ($\text{Zn}(\text{NO}_3)_2 \cdot 6\text{H}_2\text{O} \geq 99\%$) and nickel nitrate hexahydrate ($\text{Ni}(\text{NO}_3)_2 \cdot 6\text{H}_2\text{O}$, 99.99%) were

obtained from sigma Aldrich. Pure CuO/ZnO (1:1) nanocomposite was synthesized by sol gel method. In typical process, 5.94 g of $\text{Cu}(\text{NO}_3)_2 \cdot 3\text{H}_2\text{O}$ and 7.32 g of $\text{Zn}(\text{NO}_3)_2 \cdot 6\text{H}_2\text{O}$ materials were dissolved in 100 mL of deionized water with continuous stirring for 10 min. Then, 9.4 g of citric acid was added to the above solution followed by addition of 3.1 mL of ethylene glycol with vigorous stirring for 30 min. After that, the solution was heated at 95 °C with constant stirring for 120 min to form the gel. The produced gel was further heated up to 160 °C in order to get a dried gel. The obtained powder was calcined at 400 °C in electric furnace for 3 h to produce CuO/ZnO composite. The same method was used to prepare 4 and 6 wt% Ni-doped CuO/ZnO composites through addition of desired weights of $\text{Ni}(\text{NO}_3)_2 \cdot 6\text{H}_2\text{O}$ to $\text{Cu}(\text{NO}_3)_2 \cdot 3\text{H}_2\text{O}$ – $\text{Zn}(\text{NO}_3)_2 \cdot 6\text{H}_2\text{O}$ solution.

2.2 Characterization and gas sensing measurements

The crystal structure of pure, 4 and 6 wt% Ni-doped CuO/ZnO composites were studied by X-ray diffraction technique (XRD, Pert Pro Panalytical diffractometer, $\text{CuK}\alpha$ radiation, 1.5460 Å). The Fourier-transform infrared (FT-IR) spectra of pure, 4 and 6 wt% Ni-doped CuO/ZnO composites were obtained using Nicolet 380 spectrometer. The morphology and elemental composition of pure, 4 and 6 wt% Ni-doped CuO/ZnO composites were investigated by scanning electron microscope (Quanta 250 FEG) and energy dispersive X-ray unit. The optical characteristics and the band gap energy of pure, 4 and 6 wt% Ni-doped CuO/ZnO composites were identified by via JASCO spectrophotometer (V-570 UV-Vis-NIR). The gas sensing properties of pure, 4 and 6 wt% Ni-doped CuO/ZnO pellets for ethanol detection were measured through using LCR meter (Hioki 3532-50) at applied voltage of 5 V and frequency of 10 kHz. The sensor pellet was placed in closed glass cell chamber. The exact concentrations of ethanol gas were achieved through injection of a certain volume of ethanol using a micro-syringe. The sensitivity (S) of pure, 4 and 6 wt% Ni-doped CuO/ZnO samples were estimated at different temperatures (25–300 °C) using the following relation:

$$\text{Sensitivity } (S) = R_a/R_g,$$

where R_a is the resistance of sensor sample in air atmosphere while R_g is the resistance of sensor sample in air containing ethanol gas.

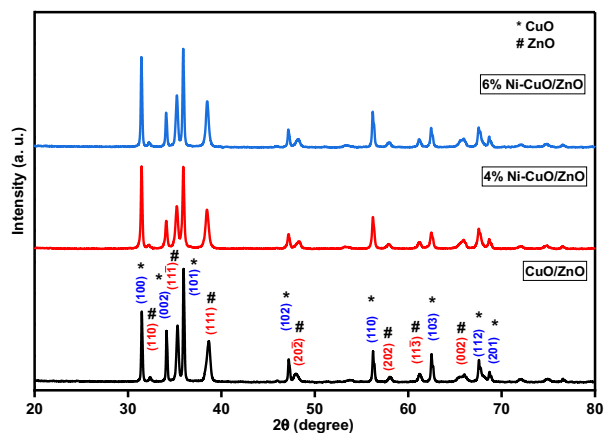


Fig. 1 X-ray diffraction patterns of pure and Ni-doped CuO/ZnO nanocomposites calcined at 400 °C for 3 h

3 Results and discussion

3.1 X-ray diffraction (XRD) analysis

Figure 1 illustrates the X-ray diffraction (XRD) patterns of pure, 4 and 6 wt% Ni-doped p-CuO/n-ZnO heterostructures synthesized by sol gel method. The recorded diffraction peaks for all samples were exactly indexed to monoclinic phase of CuO structure (JCPDS card No. 48-1548, space group C2/c) and wurtzite hexagonal phase of ZnO structure (JCPDS card No. 36-1451, space group P63mc). Herein, the diffraction peaks of pure CuO/ZnO located at $2\theta = 32.368^\circ, 35.302^\circ, 38.634^\circ, 47.973^\circ, 58.052^\circ, 61.231^\circ$ and 65.802° were assigned to (110), (11-1), (111), (20-2), (202), (11-3) and (002) crystallographic planes of monoclinic CuO component while the XRD peaks positioned at $2\theta = 31.474^\circ, 34.124^\circ, 35.952^\circ, 47.219^\circ, 56.236^\circ, 62.493^\circ, 67.742^\circ$ and 68.710° were indexed to (100), (002), (101), (102), (110), (103), (112), and (201) crystallographic planes of hexagonal ZnO component, respectively. Analogous XRD diffraction peaks with the same sequence were detected for 4 and 6 wt% Ni-doped CuO/ZnO composites. Also, it can be

seen that there is no any diffraction peaks linked to any impurities or secondary phases, verifying the synthesis of CuO/ZnO composites with high purity. The XRD peaks of all samples reveal good intensity, indicating to good crystallinity of the powders. The phase ratio, lattice parameters and unit cell volume of pure, 4 and 6 wt% Ni-doped CuO/ZnO nanocomposites were estimated and the obtained data are presented in Table 1. The phase ratios of the CuO and ZnO components was found to be close to 50% for each one which are nearby to the desired values applied in the preparation method (1:1), Table 1. For pure CuO/ZnO composite, the unit cell volume of CuO component was identified to be 81.0782 \AA^3 while that of ZnO component was detected to be 47.5129 \AA^3 . Due to incorporation of 4 wt% Ni ions, the unit cell volume of CuO component was reduced to 80.9963 \AA^3 while that of ZnO phase was reduced to 47.5054 \AA^3 . In case of 6 wt% Ni ions doping, the unit cell volume of CuO and ZnO structures was decreased to 80.9369 \AA^3 and 47.4616 \AA^3 , respectively. In the six fold coordination, the ionic radii of Cu^{2+} , Zn^{2+} and Ni^{2+} cations were 0.73 Å, 0.74 Å and 0.69 Å, respectively. Thus, the effective substitution of Cu^{2+} and Zn^{2+} sites of CuO/ZnO composite by Ni^{2+} ions, leading to the observed decreases in unit cell volume of both components. Based on Scherrer formula [52], the crystallite size of CuO and ZnO components of pure, 4 and 6 wt% Ni-doped CuO/ZnO nanocomposites were estimated as shown in Table 1. The crystallite sizes of the composites powders were found to be within 24–35 nm, which confirm the small nano-sized of the particles.

3.2 Morphological and compositional study: SEM-EDX

Figure 2 displays the scanning electron microscope (SEM) of pure, 4 and 6 wt% Ni-doped CuO/ZnO heterostructures produced by calcination at 400 °C.

Table 1 Phase ratio, lattice parameters (a, b, c), unit cell volume (V) and crystallite size D (nm) of pure and Ni-doped CuO/ZnO nanocomposites

Sample	Phase	Ratio %	a Å	b Å	c Å	V (Å) ³	D (nm)
CuO/ZnO	CuO	51.5	4.7477	3.4105	5.1483	81.0782	27
	ZnO	48.5	3.2478	3.2478	5.2010	47.5129	24
4 wt% Ni	CuO	48.5	4.6841	3.4195	5.1265	80.9963	35
	ZnO	51.5	3.2473	3.2473	5.2020	47.5054	29
6 wt% Ni	CuO	49.8	4.6822	3.4209	5.1225	80.9369	32
	ZnO	50.2	3.2468	3.2468	5.1989	47.4616	27

For pure CuO/ZnO heterostructure, the SEM image shows the formation of homogenous and well distribution spherical particles in contact with each other. Owing to incorporation of 4 wt% Ni ions, some rods structure were seen in the SEM micrograph of CuO/ZnO heterostructure besides major semi-spherical particles. In case of incorporation of 6 wt% Ni ions, the SEM micrograph demonstrates that the content of the rods structure shape was increased in the CuO/ZnO composite and the other particles become very fine with spherical shape. It appears that the addition of Ni²⁺ ions to CuO/ZnO heterostructure act as seeds for ZnO rods growth which in accordance with some previous published studies [53]. Figure 3 demonstrates the energy dispersive X-ray (EDX) spectra

of pure and 4% Ni-doped CuO/ZnO powders. The elemental content of both composites verified the occurrence of Cu, Zn and O elements besides Ni element in case of the doped sample. The weight% of the Ni element as a dopant was measured to be 2.91 wt% which is comparable with the used value during the preparation under the accepted error of EDX analysis.

3.3 FTIR analysis

Figure 4 displays the Fourier-transform infrared (FTIR) spectra of pure, 4 and 6 wt% Ni-doped CuO/ZnO heterostructures within wavenumber of 2000–400 cm⁻¹. All the synthesized composites

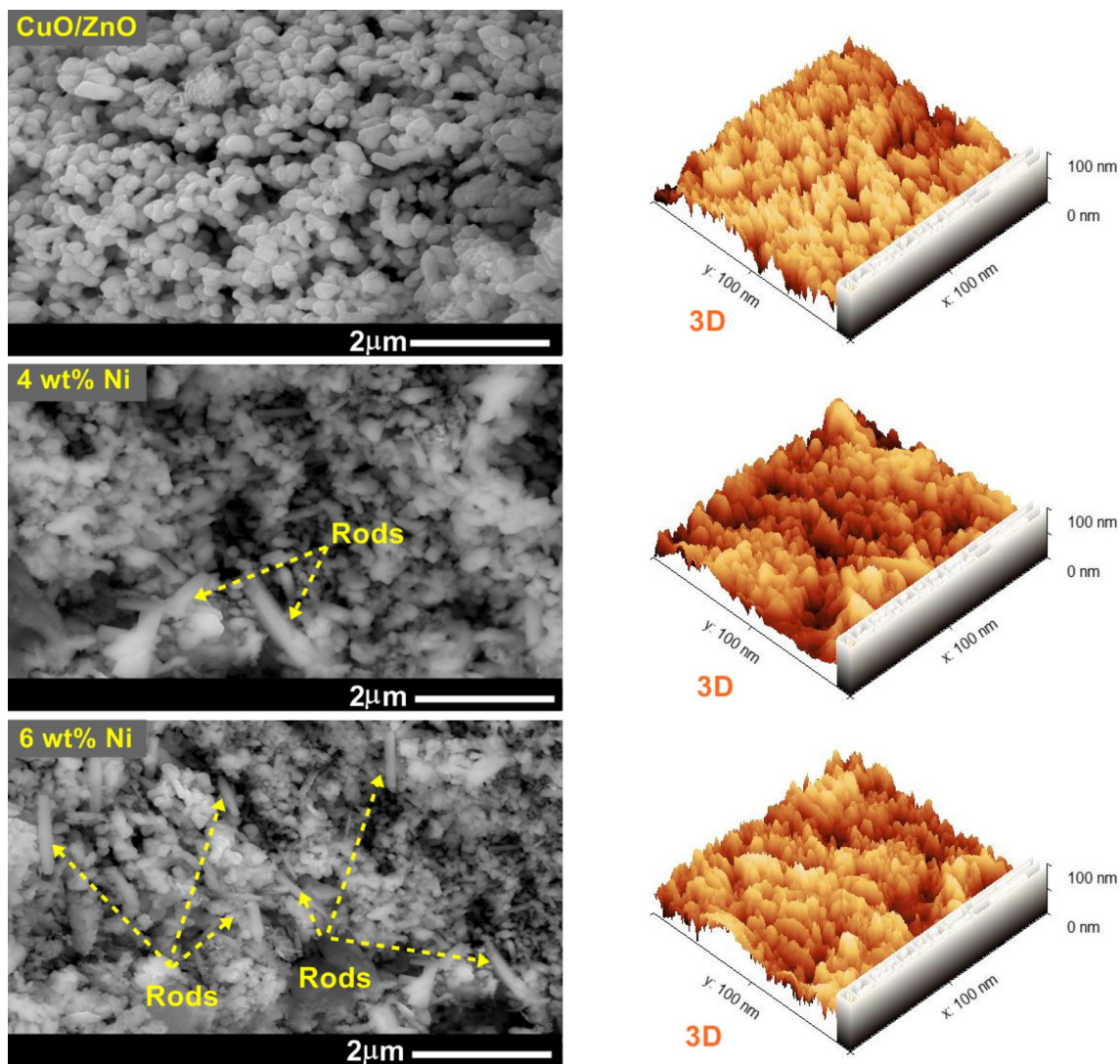


Fig. 2 Scanning electron microscope and 3D view images of pure and Ni-doped CuO/ZnO nanocomposites calcined at 400 °C for 3 h

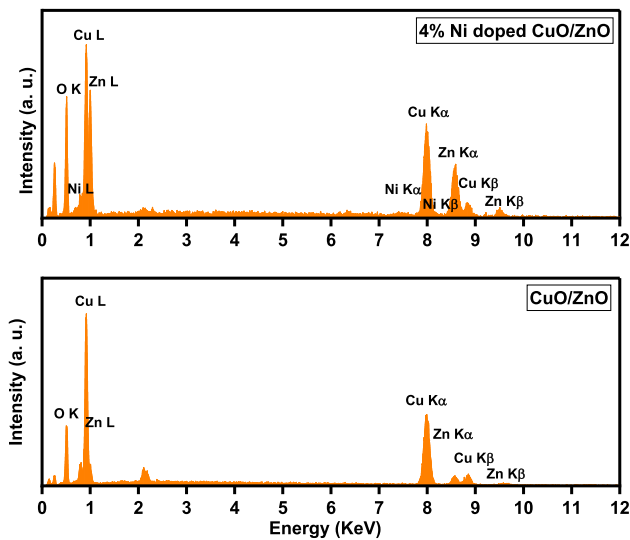


Fig. 3 Energy dispersive X-ray spectra of pure and 4 wt% Ni-doped CuO/ZnO nanocomposites

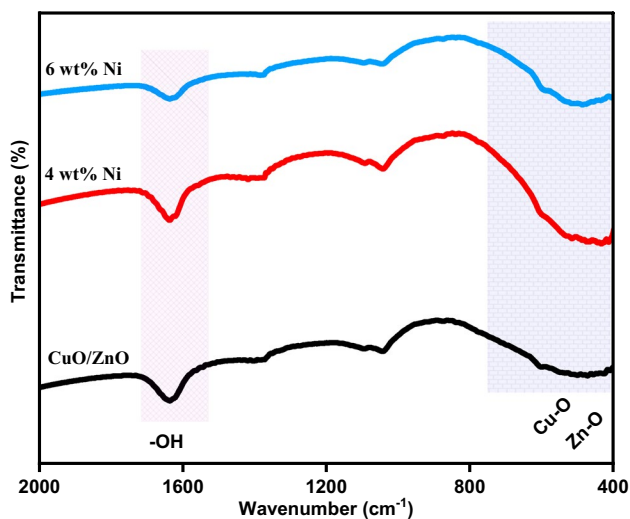


Fig. 4 FTIR vibrational absorption spectra of pure and Ni-doped CuO/ZnO nanocomposites

displayed approximately analogous IR spectra. The vibration absorption band detected at 1634 cm^{-1} can be attributed to the -OH bending vibration of adsorbed water on CuO/ZnO composites surface [54, 55]. Commonly, the typical vibration absorption bands of CuO and ZnO components were noticed within the wavenumber below 1000 cm^{-1} , Fig. 4. As reported [54], pure CuO structure revealed three main FTIR vibrational absorption bands owing to Cu–O bond vibrations situated almost at 603 cm^{-1} , 497 cm^{-1} , and 432 cm^{-1} . In case

of pure ZnO structure, the main vibrational absorption band can be detected around 450 cm^{-1} due to the stretching vibration of Zn–O bond [55]. In our CuO/ZnO heterostructures, the vibration absorption bands of Cu–O and Zn–O components overlap to give broad shape with two observed peaks at nearly 595 cm^{-1} linked to Cu–O structure and at 439 cm^{-1} related to ZnO component.

3.4 Band gap and optical characteristics of CuO/ZnO heterostructures

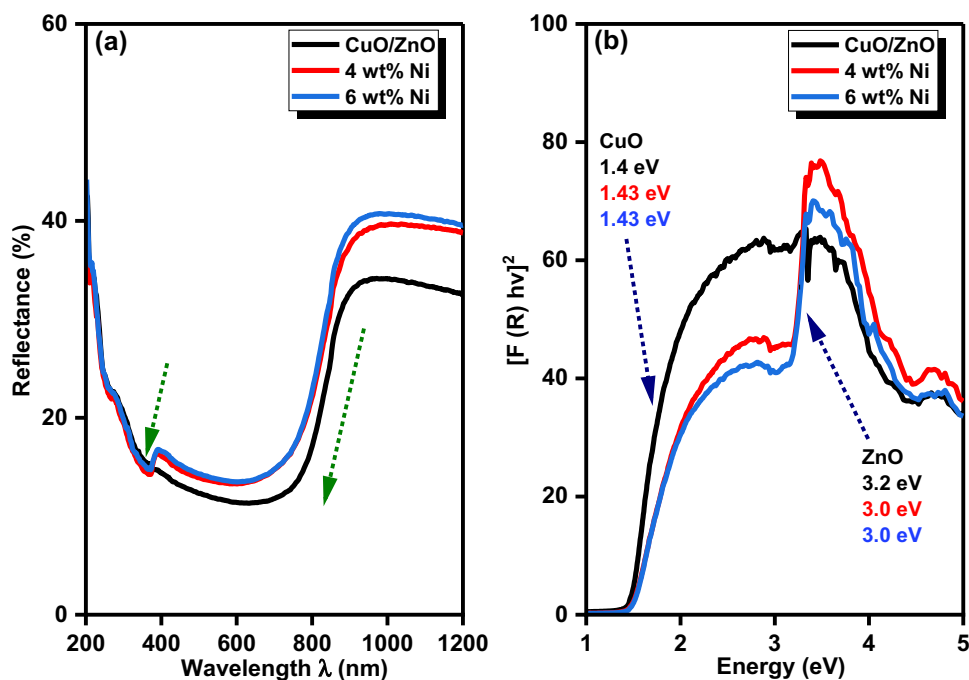
Figure 5 demonstrate the diffuse reflectance curves and Kubelka–Munk plots for band gap estimation of pure, 4 and 6 wt% Ni-doped CuO/ZnO nanocomposites. As illustrated in Fig. 5a, the diffuse reflectance curves of pure, 4 and 6 wt% Ni-doped CuO/ZnO nanocomposites possess two reduction in intensity of reflectance (%) related to band gap absorption of CuO and ZnO components. The reduction in intensity of reflectance in the wavelength region within $750\text{--}850\text{ nm}$ was linked to the absorption band gap energy of CuO component while the reduction in intensity of reflectance within the wavelength region of $420\text{--}380\text{ nm}$ was indexed to ZnO component. The obtained results of the diffuse reflectance was used to estimate the exact value of the band gap energy of pure, 4 and 6 wt% Ni-doped CuO/ZnO nanocomposites using Kubelka–Munk and Tauc equations [49, 50]:

$$F(R) = (1 - R)^2 / 2R = \alpha(\lambda) / S(\lambda) \quad (1)$$

$$\alpha = A(h\nu - E_g)^n / h\nu, \quad (2)$$

where R signifies to the percentage of the reflected light, $F(R)$ indicates to Kubelka–Munk function, α is the absorption coefficient, S is the scattering coefficient, E_g represents the band gap energy and $h\nu$ energy of incident wavelength. The relation of the $[F(R) h\nu]^2$ on the Y axis against energy ($h\nu$) on the X-axis yields the band gap energy as shown in Fig. 5 (b). The nanocomposite of the pure CuO/ZnO exhibits two band gap energies with values of 1.4 and 3.2 eV and both can be exactly indexed to CuO and ZnO components in agreement with the reported data, respectively [56–59]. Owing to addition of 4 or 6 wt% Ni ions to CuO/ZnO nanocomposite, the band gap energy of ZnO component was reduced to 3.0 eV while the band gap of CuO component was blue shifted to 1.43 eV. This effect of

Fig. 5 Illustrates a change of reflectance (%) with wavelength (200–1200 nm) and **b** Kubelka–Munk plot for band gap determination of pure and Ni-doped CuO/ZnO nanocomposites



the Ni ions on the band gap energy of CuO and ZnO components point out that the Ni ions have been structural incorporated into their lattices. It can be noticed that the Ni ions exhibit opposite influence on both components (blue shift and red shift). The red shift in case of n-type ZnO component can be assigned to s-d and p-d exchange interactions between the localized electrons of the Ni ions and the band electrons [60]. Furthermore, the formation of rods structure related to ZnO after Ni ions doping may be has a certain effect in these reductions of the band gap [61]. Whereas, the blue shift in case of CuO component can be attributed to Ni replacement at the Cu sites into the CuO lattice in accordance with the previous study on Ni-doped CuO [62].

3.5 Gas sensing characteristics of pure and Ni-doped CuO/ZnO heterostructures

Figure 6a shown the gas sensing response of pure, 4 and 6 wt% Ni-doped CuO/ZnO heterostructures towards 100 ppm ethanol gas at different temperature. For pure CuO/ZnO heterostructure, the sensitivity of the sensor was increased with increasing the temperature and attains the maximum value of 43 at 250 °C. Interestingly, the addition of 4 wt% Ni greatly enhanced the sensitivity of CuO/ZnO heterostructures to 97 and also reduced the working temperature to 225 °C. As well, the incorporation

of 6 wt% Ni ions into CuO/ZnO heterostructure improved the sensitivity value to reach to 74.5 at operating temperature of 225 °C. The findings indicate that the Ni ions doping is effective in enhancing the sensitivity value of CuO/ZnO heterostructure as well as reduces the working temperature at suitable concentration of 4 wt%. The sensitivity of the pure, 4 and 6 wt% Ni-doped CuO/ZnO heterostructures at room temperature is shown in Fig. 6b. At room temperature, 4 wt% Ni-doped CuO/ZnO heterostructure sensor exhibits acceptable response value to 100 ppm ethanol gas with recorded sensitivity value of 6.1. The room temperature sensitivity value of pure and 6 wt% Ni-doped CuO/ZnO sensors were identified to be 1.9 and 3.1 towards 100 ppm ethanol gas. The variation of sensitivity with ethanol gas concentrations (50–500 ppm) was tested for best sample, 4 wt% Ni-doped CuO/ZnO composite, as illustrated in Fig. 6c. The response of this sensor was increased linearly with increase ethanol concentration from 50 to 250 ppm and above this concentration the sensitivity value was moderately increased. The selectivity of the 4 wt% Ni-doped CuO/ZnO composite for ethanol gas was explored by measuring the response to methanol, acetone, propanol and CO₂ gases at operating temperature of 225 °C and gases concentration of 100 ppm. For methanol, ethanol, acetone, propanol and CO₂ gases the sensitivity value of 4

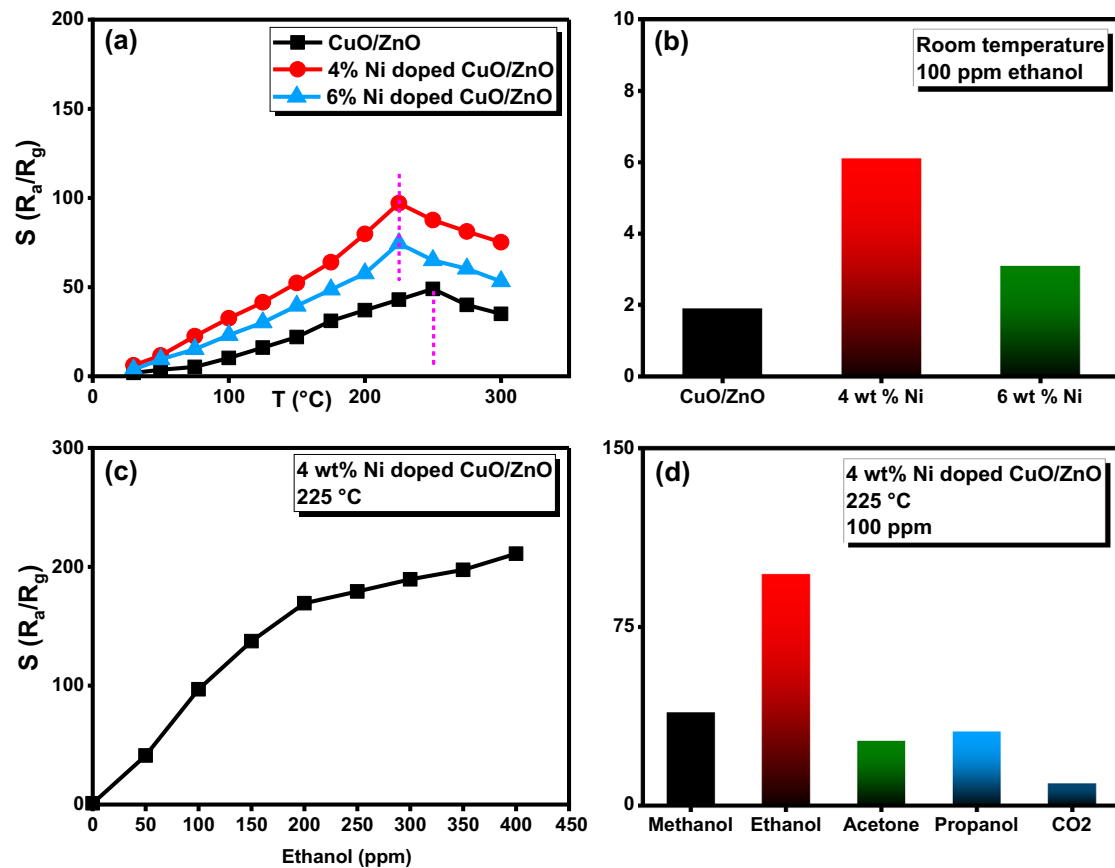


Fig. 6 Illustrates **a** sensitivity of pure and Ni-doped CuO/ZnO nanocomposites at different temperature for 100 ppm ethanol, **b** sensitivity of pure and Ni-doped CuO/ZnO nanocomposites at room temperature for 100 ppm ethanol, **c** variation of sensitivity

wt% Ni-doped CuO/ZnO composite was found to be 39, 96, 27, 31 and 9, respectively. Based on these findings we can conclude that 4 wt% Ni-doped CuO/ZnO composite has excellent response and selectivity towards ethanol gas at working temperature of 225 °C.

The response time, recovery time and stability are important issues, since these parameters can limit the applicability of the sensor material. After exposed to target gas, the response time of the tested gas sensor material can be defined as the time taken to attain at least 90% of the final variation in response [63, 64]. The recovery time can be definite as the time taken for the tested gas sensor material to fall to 10% of its maximum sensitivity value after the target gas was exits (exposed to air). Figure 7a displays the variation of sensitivity with time (second) for 4 wt% Ni-doped CuO/ZnO composite sensor after exposed to 100 ppm at operating temperature of 225 °C. The

with ethanol concentration of 4 wt% Ni-doped CuO/ZnO nanocomposite and **d** responses of 4 wt% Ni-doped CuO/ZnO sensor for different gases

wt% Ni-doped CuO/ZnO sensor displays a fast response to ethanol gas and attains nearly 90% of sensitivity in 20 s. As illustrated in Fig. 7b, the recovery time of this sensor was found to be 15 s. The high stability of the tested sensor is a critical factor to decide its practical uses. To explore the stability, the response of the 4 wt% Ni-doped CuO/ZnO composite was measured for 28 days (every 3 days) at concentration of 100 ppm ethanol gas and operating temperature of 225 °C, Fig. 7c. The measured values illustrate that the sensor has approximately constant response during this period. These results reflect the excellent stability, fast response and recovery time of the synthesized 4 wt% Ni-doped CuO/ZnO composite sensor.

The sensing mechanism of 4 wt% Ni-doped CuO/ZnO composite is mainly depends on the interaction between ethanol gas and the adsorbed oxygen species on the particles surface and can be summarized

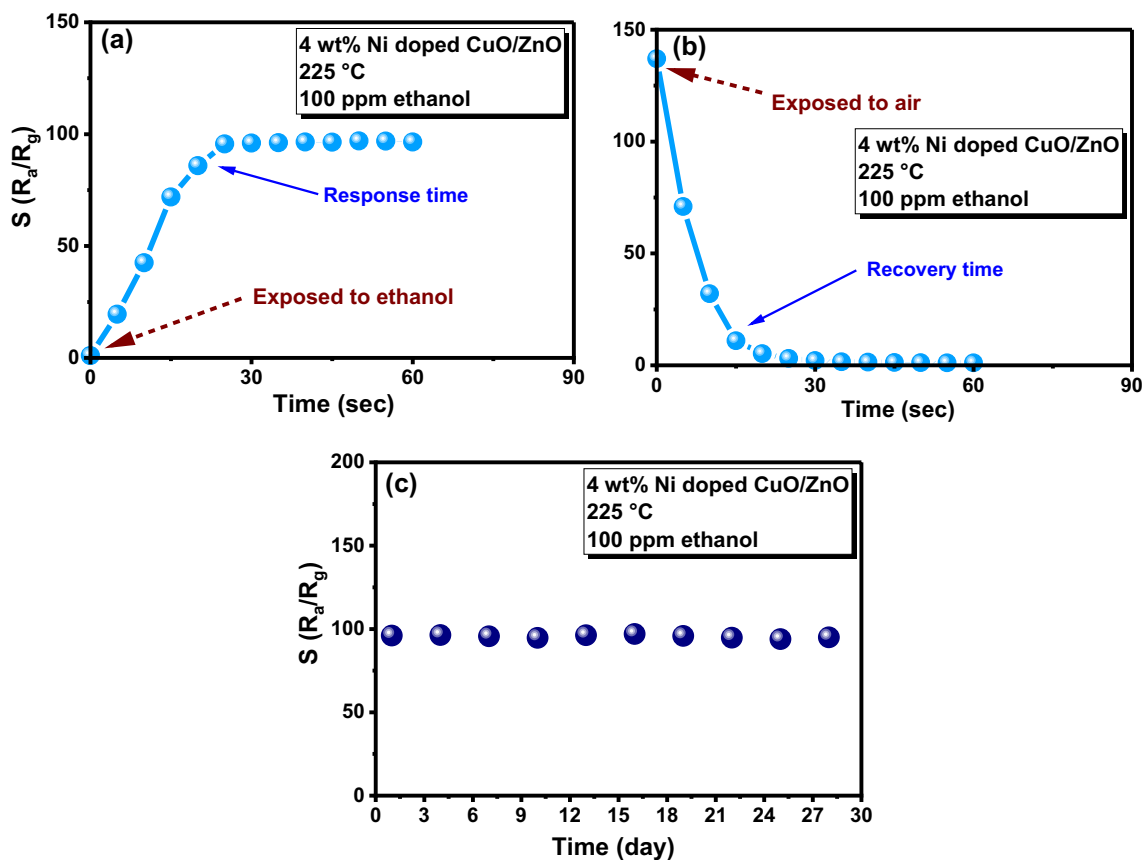


Fig. 7 Illustrates **a** response time of 4 wt% Ni-doped CuO/ZnO nanocomposite at 225 °C after exposed to 100 ppm ethanol, **b** recovery time of 4 wt% Ni-doped CuO/ZnO nanocomposite

at 225 °C after exposed to air and **c** stability of 4 wt% Ni-doped CuO/ZnO nanocomposite for 100 ppm ethanol during measurements for 28 days

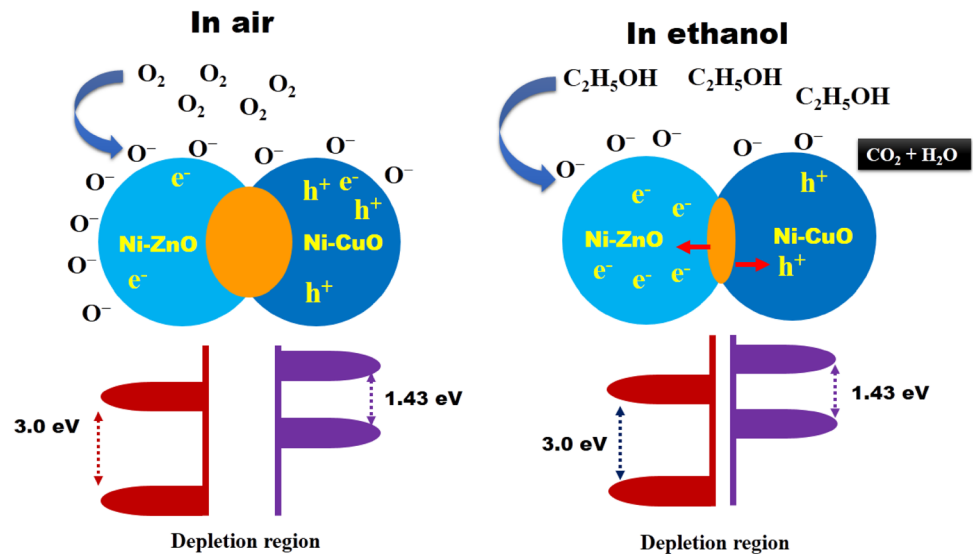
in two steps as illustrated in Fig. 8. Firstly, when 4 wt% Ni-doped CuO/ZnO composite was heated under air atmosphere, the oxygen molecules (O_2) were adsorbed and convert to oxygen ions (O^- , O^{2-}) through trapping the electrons from the conduction band of the sensor [30]. Secondly, after exposed to ethanol gas, the molecules of ethanol interact with the adsorbed oxygen ions (O^- , O^{2-}) present on the surface of the sensor and return the released electrons back to the conduction band, consequently decreasing the resistance of the sample [30]. The exposing of Ni-doped CuO/ZnO to ethanol gas will inject the trapped electrons by adsorbed oxygen ions into the material. With respect to ZnO, these reactions will add more electrons to it and in case of CuO the released electrons will consume the holes and also leads to excess electrons in ZnO, thus reduce the thickness of the depletion region. Owing to the presence of p–n heterojunctions, the consumed holes in

CuO would rapidly be supplemented from the electron depletion layer at p–n junctions. During this process, the holes in the ZnO/CuO heterojunction travel to CuO across the hetero-contact interface and the electrons move into the conduction band, which in turn increase the charge carrier concentration, causing a decrease in resistivity. The enhanced sensitivity of Ni-doped CuO/ZnO composite can be attributed to Ni doping and rods structure formation. The doping by Ni ions can yields more oxygen vacancies as well leads to rods structure formation which enhance the adsorbed oxygen concentration and consequently increase the gas sensing characteristics.

4 Conclusions

In this study, highly crystalline pure, 4 and 6 wt% Ni-doped CuO/ZnO heterostructures were synthesized via sol–gel method to detect ethanol gas. The

Fig. 8 Schematic illustration of the gas sensing mechanism of the 4 wt% Ni-doped CuO/ZnO nanocomposite sensor



results of XRD confirmed the formation of monoclinic CuO and hexagonal ZnO phases without presence of any impurities. Based on SEM images, the incorporation of Ni ions leads to formation of some rods structure besides major fine semi-spherical particles. The gas sensing measurements of pure, 4 and 6 wt% Ni-doped CuO/ZnO heterostructures were tested for ethanol as well as methanol, acetone, propanol and CO_2 gases. The obtained results illustrate that 4 wt% Ni-doped CuO/ZnO sensor has the highest response value of 97 towards 100 ppm ethanol gas with high selectivity. This sensor exhibits good linear relation between sensitivity and ethanol gas concentration within 50–250 ppm. As well, it possesses a fast response time of 20 s and small recovery time of 15 s with excellent stability for 28 days. This findings point out that Ni-doped CuO/ZnO hetero-junction is a highly promising sensitive structure for ethanol gas detection.

Author contributions

The submission of the manuscript has been approved by all authors. All authors have equal contributions in preparing the manuscript including experimental, writing, discussion and revision.

Funding

The authors declare that no funds, grants, or other support were received during the preparation of this manuscript.

Data availability

The datasets generated during and/or analyzed during the current study are available from the corresponding author on reasonable request.

Declarations

Conflict of interest The authors declare that they have no known competing financial interests or personal relationships that could have appeared to influence the work reported in this paper.

References

1. S. Dhall, B.R. Mehta, A.K. Tyagi, K. Sood, *Sens. Int.* **2**, 100116 (2021)
2. Z. Wang, L. Zhu, J. Wang, R. Zhuang, P. Mu, J. Wang, W. Yan, *RSC Adv.* **12**, 24614–24632 (2022)
3. M. Hjiri, F. Bahanan, M.S. Aida, L. El Mir, G. Neri, *J. Inorg. Organomet. Polym. Mater.* **30**, 4063–4071 (2020)

4. Z. Wang, Y. Wang, J. Yan, B. Liu, Y. Chen, Y. Tian, *Mater. Adv.* **3**, 6728–6741 (2022)
5. A.A. Vasiliev, V.V. Malyshev, *Sens. Actuators B* **189**, 260–267 (2013)
6. L. Jiang, S. Lv, W. Tang, L. Zhao, C. Wang, J. Wang, T. Wang, X. Guo, F. Liu, C. Wang, P. Sun, C. Zhang, J. Zheng, G. Lu, *Sens. Actuators B* **345**, 130321 (2021)
7. L.-Y. Zhu, L.-X. Ou, L.-W. Mao, X.-Y. Wu, Y.-P. Liu, H.-L. Lu, *Nano-Micro Lett.* **15**, 89 (2023)
8. G.J. Thangamani, K. Deshmukh, T. Kovářik, N.A. Nambiraj, D. Ponnamma, K.K. Sadasivuni, H.P.S. Abdul Khalil, S.K.K. Pasha, *Chemosphere* **280**, 130641 (2021)
9. M. Morsy, I.S. Yahia, H.Y. Zahran, M. Ibrahim, J. Inorg. Organomet. Polym. Mater. **29**, 416–422 (2019)
10. A. Nur'aini, I. Oh, *RSC Adv.* **10**, 12982–12987 (2020)
11. E.A. Silva, M.L. Braunger, A. Gregori, C.A. Olivati, *SN Appl. Sci.* **1**, 200 (2019)
12. J. Alzeer, K. Abou Hadeed, *Trends Food Sci. Technol.* **58**, 14–20 (2016)
13. J. Li, Q. Ding, X. Mo, Z. Zou, P. Cheng, Y. Li, K. Sun, Y. Fu, Y. Wang, D. He, *RSC Adv.* **11**, 39130–39141 (2021)
14. S. Ud Din, M. ul Haq, R. Khatoon, X. Chen, L. Li, M. Zhang, L. Zhu, *RSC Adv.* **10**, 21940–21953 (2020)
15. N. Jain, N.K. Puri, *J. Alloys Compd.* **955**, 170178 (2023)
16. Y. Tan, J. Zhang, *Physica E* **147**, 115604 (2023)
17. A. Hussain, M.N. Lakhani, I.A. Soomro, M. Ahmed, A. Hanan, A.A. Maitlo, I. Zehra, J. Liu, J. Wang, *Physica E* **147**, 115574 (2023)
18. P. Jahanshahi, Q. Wei, Z. Jie, E. Zalnezhad, *Biotechnol. Bioprocess Eng.* **23**, 394–404 (2018)
19. E.P. Nahirny, M.F. Bergamini, L.H. Marcolino-Junior, *J. Electroanal. Chem.* **877**, 114659 (2020)
20. Q. Wang, J. Bai, Q. Hu, J. Hao, X. Cheng, J. Li, E. Xie, Y. Wang, X. Pan, *Sens. Actuators B Chem.* **308**, 127668 (2020)
21. S. Tyagi, M. Chaudhary, A.K. Ambedkar, K. Sharma, Y.K. Gautam, B.P. Singh, *Sens. Diagn.* **1**, 106–129 (2022)
22. N.A. Isaac, I. Pikaar, G. Biskos, *Microchim. Acta.* **189**, 196 (2022)
23. N. Chakraborty, S. Mondal, *J. Mater. Chem. C* **10**, 1968–1976 (2022)
24. E. Salih, A.I. Ayesh, *Physica E* **131**, 114736 (2021)
25. S. Srivastava, P. Pal, D.K. Sharma, S. Kumar, T.D. Senguttuvan, B.K. Gupta, *ACS Mater. Au.* **2**, 356–366 (2022)
26. N.K. Chowdhury, B. Bhowmik, *Nanoscale Adv.* **3**, 73–93 (2021)
27. Y.N. Colmenares, W. Correr, B.S. Lima, V.R. Mastelaro, *Thin Solid Films.* **703**, 137975 (2020)
28. U.T. Nakate, Y.T. Yu, S. Park, *Sens. Actuators B Chem.* **344**, 130264 (2021)
29. S.M. Majhi, H.-J. Lee, H.-N. Choi, H.-Y. Cho, J.-S. Kim, C.-R. Lee, Y.-T. Yu, *CrystEngComm* **21**, 5084–5094 (2019)
30. M. Poloju, N. Jayababu, M.V.R. Reddy, *Mater. Sci. Eng.* **227**, 61–67 (2018)
31. W.J. Moon, J.H. Yu, G.M. Choi, *Sens. Actuators B* **87**, 464–470 (2002)
32. R. Leghrib, A. Felten, J.J. Pireaux, E. Llobet, *Thin Solid Films.* **520**, 966–970 (2011)
33. C. Cheng, C. Chen, H. Zhang, Y. Zhang, *Mater. Sci. Semiconduct. Process.* **146**, 106700 (2022)
34. X. Wang, S. Li, L. Xie, X. Li, D. Lin, Z. Zhu, *Ceram. Int.* **46**, 15858–15866 (2020)
35. X. Zhang, P. Guo, Q. Pan, K. Shi, G. Zhang, *J. Alloys Compd.* **727**, 514–521 (2017)
36. S. Gao, Y. Zhao, W. Wang, J. Zhao, X. Wang, *Sens. Actuators B* **371**, 132515 (2022)
37. Y. Ji, N. Zhang, J. Xu, Q. Jin, X. San, X. Wang, *Ceram. Int.* **49**, 17354–17362 (2023)
38. T. Zhou, T. Zhang, R. Zhang, Z. Lou, J. Deng, G. Lu, L. Wang, *Sens. Actuators B* **255**, 745–753 (2018)
39. A.M.M. Musa, M. Rasadujjaman, M.A. Gafur, Jamil, *Thin Solid Films.* **773**, 139838 (2023). A. T. M. K
40. A. Din, K.S. Karimov, K. Akhtar, A.M. Asiri, S. Gul, M.I. Khan, M.A. Khan, E.M. Bakhsh, S.B. Khan, *Inorg. Chem. Commun.* **145**, 109897 (2022)
41. H. Su, H. Li, H. Lin, X. Shi, Y. Du, Y. Luo, H. Deng, *Int. J. Biol. Macromol.* **206**, 653–660 (2022)
42. J.D. Choi, G.M. Choi, *Sens. Actuators B* **69**, 120–126 (2000)
43. Y. Chen, Z. Shen, Q. Jia, J. Zhao, Z. Zhao, H. Ji, *RSC Adv.* **6**, 2504–2511 (2016)
44. Y. Tang, Y. Huang, H.-Y. Zou, L. Wu, Z.-L. Xiao, J.-L. Zeng, L.-X. Sun, D. Yu, Z. Cao, *Anal. Methods.* **14**, 2866–2875 (2022)
45. H. Ren, H. Weng, P. Zhao, R. Zuo, X. Lu, J. Huang, *Front. Mater. Sci.* **16**, 220583 (2022)
46. X. Liu, Y. Sun, M. Yu, Y. Yin, B. Du, W. Tang, T. Jiang, B. Yang, W. Cao, M.N.R. Ashfold, *Sens. Actuators B* **255**, 3384–3390 (2018)
47. Y.-B. Zhang, J. Yin, L. Li, L.-X. Zhang, L.-J. Bie, *Sens. Actuators B* **202**, 500–507 (2014)
48. M.-R. Yu, G. Suyambrakasam, R.-J. Wu, M. Chavali, *Mater. Res. Bull.* **47**, 1713–1718 (2012)
49. C. Qin, Y. Wang, Y. Gong, Z. Zhang, J. Cao, *J. Alloys Compd.* **770**, 972–980 (2019)
50. M. Akbari-Saatlu, M. Procek, C. Mattsson, G. Thungström, T. Törndahl, B. Li, J. Su, W. Xiong, H.H. Radamson, *ACS Appl. Nano Mater.* **5**, 6954–6963 (2022)
51. S. Zhao, Y. Shen, F. Hao, C. Kang, B. Cui, D. Wei, F. Meng, *Appl. Surf. Sci.* **538**, 148140 (2021)

52. I.H. Mejri, K. Omri, I. Ghilouf, J.P.B. Silva, M.J.M. Gomes, L. El Mir, *Appl. Phys. A* **129**, 210 (2023)
53. S. Husain, L.A. Alkhtaby, E. Giorgetti, A. Zoppi, M.M. Miranda, *J. Lumin.* **145**, 132–137 (2014)
54. A.S. Ethiraj, D.J. Kang, *Nanoscale Res. Lett.* **7**, 70 (2012)
55. C.P. Rezende, J.B. da Silva, N.D.S. Mohallem, *Braz. J. Phys.* **39**, 248–251 (2009)
56. B.B. Salem, G. Essalah, S.B. Ameer, B. Duponchel, H. Guermazi, S. Guermazia, G. Leroy, *RSC Adv.* **13**, 6287–6303 (2023)
57. N. Alebachew, H.C.A. Murthy, B. Abdissa, T.B. Demissie, K.G. von Eschwege, E.H.G. Langner, L. Coetsee-Hugo, *RSC Adv.* **12**, 29959–29974 (2022)
58. X. Zhang, Y. Yang, W. Que, Y. Du, *RSC Adv.* **6**, 81607–81613 (2016)
59. C. Baratto, *RSC Adv.* **8**, 32038–32043 (2018)
60. H. Minhas, D. Kumar, A. Kumar, *Mater. Res. Express.* **6**, 105049 (2019)
61. A.A. Firooz, R.A. Mirzaie, F. Kamrani, *J. Struct. Chem.* **59**, 739–743 (2018)
62. R. Aydın, A. Akkaya, B. Şahin, *J. Mater. Sci.* **33**, 23806–23820 (2022)
63. N.S.A. Eom, H.-B. Cho, H.-R. Lim, T.-Y. Hwang, Y. Song, Y.-H. Cho, *RSC Adv.* **8**, 29995–30001 (2018)
64. R. Souissi, N. Bouguila, B. Bouricha, C. Vázquez-Vázquez, M. Bendahane, A. Labidi, *RSC Adv.* **10**, 18841–18852 (2020)

Publisher's Note Springer Nature remains neutral with regard to jurisdictional claims in published maps and institutional affiliations.

Springer Nature or its licensor (e.g. a society or other partner) holds exclusive rights to this article under a publishing agreement with the author(s) or other rightsholder(s); author self-archiving of the accepted manuscript version of this article is solely governed by the terms of such publishing agreement and applicable law.